In Situ Liquid Electrochemical TEM Investigation of LiMn1.5Ni0.5O4 Thin Film Cathode for Micro-Battery Applications

Ankush Bhatia, Sorina Cretu, Maxime Hallot, Nicolas Folastre, Maxime Berthe, David Troadec, Pascal Roussel, Jean Pierre Pereira-Ramos, Rita Baddour-Hadjean, C. Lethien, et al.

In situ Liquid Electrochemical TEM Investigation of $LiMn_{1.5}Ni_{0.5}O_4$ Thin Film Cathode for Micro-Battery Application

Ankush Bhatia[1,2], Sorina Cretu[2,4], Maxime Hallot[3, 4], Nicolas Folastre[2,4], Maxime Berth[3], David Troadec[3], Pascal Roussel[5], Jean-Pierre Pereira-Ramos[1], Rita Baddour-Hadjean[1], Christophe Lethien[3,4], Arnaud Demortière[2,4,6]*

[1]Institut de Chimie et des Matériaux Paris Est (ICMPE), CNRS UMR 7182 –Université Paris Est Créteil, 2-8 rue Henri Dunant, 94320 Thiais, France

[2]Laboratoire de Réactivité et de Chimie des solides (LRCS), Université de Picardie Jules Verne, CNRS UMR 7314, 33 rue Saint Leu, 80039 Amiens Cedex, France

[3]Institut d'Electronique, de Microélectronique et de Nanotechnologies, Université de Lille, Centrale Lille, ISEN, Université de Valenciennes, CNRS UMR 8520- IEMN, F-59000 Lille, France

[4]Réseau sur le stockage Electrochimique de l'Energie, CNRS FR 3459, 33 rue Saint Leu, 80039 Amiens Cedex, France

[5]Univ. Lille, CNRS, Centrale Lille, Univ. Artois, UMR 8181, Unité de Catalyse et Chimie du Solide (UCCS), F-59000 Lille, France

[6]ALISTORE-European Research Institute, CNRS FR 3104, Hub de l'Energie, 15 Rue Baudelocque, Amiens, Cedex 80039, France

Corresponding author: arnaud.demortiere@energie-rs2e.com

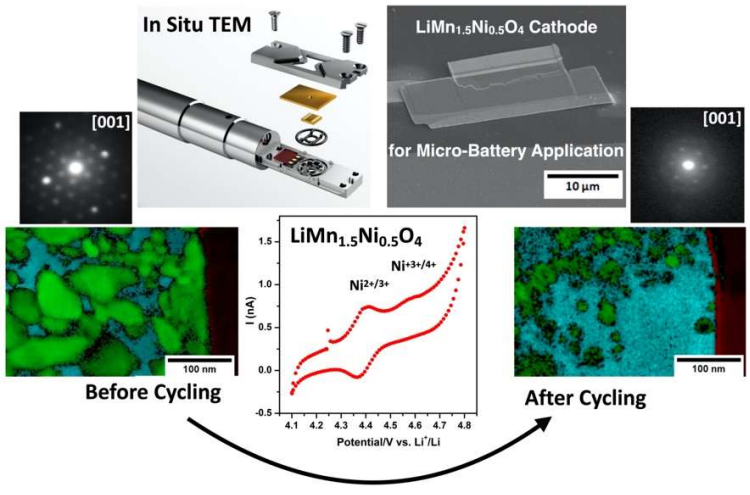

KEYWORDS: *In situ* liquid electrochemical TEM, Thin film micro-battery, FIB lamella connection to micro-chip, 4D-STEM-ASTAR, $LiMn_{1.5}Ni_{0.5}O_4$ cathode materials

Abstract: Micro-batteries are attractive miniaturized energy devices for new internet of things applications, but the lack of understanding of their degradation process during cycling hinders improving their performance. In this work, a FIB-lamella from $LiMn_{1.5}Ni_{0.5}O_4$ thin film cathode is *in situ* cycled in a liquid electrolyte inside an electrochemical TEM holder to analyze structural and morphological changes upon (de)lithiation processes. A successful procedure was set up to achieve a high-quality electrical connection between the Pt current collector of the FIB-lamella and the Pt working electrode of the microchip, which was confirmed by local 2-probe conductivity measurements. *In situ* cyclic voltammetry experiments show two redox activities at 4.41/4.37 and 4.58/4.54 V corresponding to the $Ni^{2+/3+}$ and $Ni^{3+/4+}$ couples, respectively. (S)TEM investigations of the cycled thin film reveal formation of voids and cracks, loss of contact with current collector and presence of organic decomposition products. The 4D-STEM ASTAR technique further provides key information on structural and morphological changes in the *in situ* cycled electrode, highlighting the emergence of an amorphization process and a decrease in average grain size from 20 to 10 nm. Interestingly, 4D-STEM mapping reveals an epitaxial relationship between the $LiMn_{1.5}Ni_{0.5}O_4$ layer and the Pt current collector occurring during the magnetron sputtering deposition process. The present findings, obtained for the first time through the liquid electrochemical TEM study, provide several insights explaining the capacity fade of the $LiMn_{1.5}Ni_{0.5}O_4$ thin film cathode typically observed upon cycling in a conventional liquid electrolyte.

Introduction

The need for affordable, reliable and safe energy storage systems is proliferating for applications such as plug-in hybrid/electric vehicles, stationary energy storage, portable electronic devices[1]. These applications use conventional liquid electrolyte-based rechargeable Li-ion batteries that impose restrictions on both the electrode architecture for electrochemical performance and the battery design to withstand the inherent risks of leakage and flammability. Recently, all-solid-state batteries have gained increasing interest for energy storage due to their high energy density and increased safety compared to conventional liquid electrolyte batteries[2,3]. In particular, all-solid-state thin film micro-batteries (TFB) are recognized as one of the key enabling technologies for stand-alone sensor applications such as RF-ID tags, smart cards, wearable devices as well as Internet of Things (IoT) devices[4]. However, to achieve the required performance for TFB, it is crucial to choose a positive electrode material with high storage capacity and high operating voltage[5]. Over the last few years, extensive research on TFB has mainly focused on various cathode materials, such as $LiCoO_2$[6], V_2O_5[7,8], $LiFePO_4$[9] and $LiMn_2O_4$[10], using different advanced deposition techniques like atomic layer deposition (ALD), RF magnetron sputtering, spray pyrolysis, laser beam techniques and other routes[11]. Spinel $LiMn_{1.5}Ni_{0.5}O_4$ (LMNO) shows a promising result for TFB since it offers a wide potential plateau at ~4.7 V and a theoretical capacity of ~147 $mAhg^{-1}$, which is 25 % higher than the commercially used "classical" $LiMn_2O_4$ spinel $LiMn_2O_4$[12–15]. The main drawback of LMNO is its high redox voltage, around 4.7 V, which is just above the upper limit of the stability window of commercial liquid electrolytes, resulting in the formation of a cathode-solid electrolyte interface (C-SEI), self-discharge and degradation of the electrode

material, thus affecting the overall cycle life[12]. The study on LMNO thin film configuration has already been reported by various other research groups. LMNO can be crystallized in two crystallographic structures, *i.e.* an ordered spinel ($P4_332$) and a disordered spinel ($Fd\text{-}3m$). The disordered LMNO structure is well known for its superior electrochemical performance in terms of cycle life, ionic and electronic conductivity[12]. A small number of studies have been reported on LMNO thin films. In particular, recent papers[13,14] demonstrate that deposition pressure plays an important role on the ordering of Mn-Ni in sputtered LMNO thin films and that the disordered LMNO thin film exhibits better electrochemical performance than the ordered one[15]. However, it has been reported that structural and morphological changes occur in the LMNO thin films upon cycling in a liquid electrolyte, resulting in significant capacity loss and death of the electrode[16]. Although various research groups have demonstrated that nanometer-thick metal oxide or phosphate (ZnO, ZrO_2, $AlPO_4$, Li_3PO_4) coating acting as a protective layer for high working potential electrodes reduces the capacity losses and extends the electrode cycle life[16,17,18], but no proper explanations have been provided for the key changes that occur in the positive/negative electrode layer when uncoated samples are cycled in liquid electrolyte.

The overall performance of an electrochemical system (efficiency, power density, cycle life) is highly dependent on key factors such as the crystallographic structure, morphology, and chemical composition of electrode materials. A wide variety of *in situ* characterization techniques have been implemented to better understand the processes that occur at different scales during the electrochemical process, such as X-ray diffraction, Raman spectroscopy, neutron diffraction and, SEM[19–26]. While discussing battery cycle

life, it is important to broaden the picture beyond the activities taking place at the electrode-electrolyte interface and to include rich underlying phenomena such as changes in grain boundaries, crystal sizes, percolation networks, SEI layers and fine-scale defects. Hence, advanced characterization techniques usable in TEM, with which structural and chemical properties can be studied at different scales, are of great interest to improve material combination and synthesis strategies[27]. From recent years, *in situ* liquid electrochemical TEM has gained wide interest for getting better insight into the changes in active materials during the evolution of their electrochemical performance. The (de)lithiation and degradation mechanisms can be indeed monitored by real time imaging, with high spatial resolution and high speed recording[28–30]. Over the last decade, the use of two types of electrochemical devices, sealed liquid cell and open solid-state cell, has paved the way for challenging *in situ* and *operando* experiments, allowing direct observation of physicochemical transformations of battery materials[31,32] Based on the specific design of both *in situ* cell type, the limitations and requirements are drastically different. Sealed cells allow environmental TEM studies under ambient conditions, using conventional liquid electrolyte, while open cells permitting to cycle solid materials in a specific zone of interested[21,33]. A large variety of *in situ* TEM studies[34,35] in high vacuum condition were reported, in which a TEM holder equipped of metallic tips capable of piezo-actuated motion is used to contact lithium metal source (with LiO_2 layer as electrolyte) to active materials prepared either as a FIB lamella or deposed in a TEM grid[36]. Yamamoto *et al.*[37] first reported, using electron holography, the observations of electric potential distribution at the $LiCoO_2$ solid electrolyte interface during *in situ* electrochemical cycling. In another recent work, Wang *et al.*[38] used STEM-EELS mapping technique to reveal the

formation of Li_2O/Li_2O_2 as oxygen evolution reaction products in $LiCoO_2$ electrode, which causes the rapid capacity decay during the operation of all-solid state TFB. Unocic *et al.*[39] have recently reported the use of *in situ* STEM in high-resolution mode to provide unique insights into dynamically evolving electrochemical reactions at electrode/electrolyte interface in their native electrolyte environment. Dupont *et al.*[40] demonstrated the first *ex situ* TEM observation of "nanobatteries" obtained by FIB cross-section of a TFB. Huang *et al.*[41] developed *in situ* TEM implemented with a micro-electromechanical system (MEMS) heating device to study the precipitation and decomposition of Li_2S at high temperature in an all-solid-state Li-S batteries. The *in situ* electrochemical TEM is a powerful multimodal tool, with high spatiotemporal resolution, for fundamental investigations of electro-chemo-mechanical phenomena linked to the reactions and degradations occurring in the electrode, the solid electrolyte and various interfaces.

The present work reports the first *in situ* TEM investigation on a LMNO thin film cathode to analyze the local morphological and structural changes occurring upon cycling in liquid electrolyte and involved in the capacity fade. Key information extracted from the *in situ* study will help to enhance the reliability and improve the quality of such a micro-device. This paper will be organized into four parts. The first section presents the structural characterization of the pristine LMNO thin film and its electrochemical properties in liquid electrolyte in a conventional electrochemical cell. Then, the engineering challenges are described and a solution for producing suitable FIB samples for the TEM study is proposed, as demonstrated by 2-probe conductivity measurements that assess the electrical contact quality. The third and fourth sections report the *in situ* TEM investigations of the pristine and cycled LMNO FIB lamella, respectively.

Crystallographic phase and orientation maps based on a series of electron diffraction patterns highlight the interest of the 4D STEM-ASTAR technique[42] to locally characterize the source of defects responsible for the capacity fade of LMNO thin films in liquid electrolyte.

Result and Discussion

Characterization of the pristine LMNO thin film

Figure 1a shows the SEM image of the cross-section of the RF-sputtered 400 nm-thick LMNO thin film deposited on $Si/Al_2O_3/Pt$ substrate at a working pressure of 0.025 mbar followed by annealing at 700 °C for 2 hours. The 100 nm thick Al_2O_3 coating plays the role of diffusion barrier layer between the Pt current collector and silicon wafer to avoid the formation of undesirable insulator Pt Si phase during the annealing process[13]. The SEM image clearly shows the densely packed grain morphology of the LMNO layer[14,43].

Ordered and disordered crystal structures of LMNO can be easily discriminated by Raman spectroscopy since this technique is sensitive to the different local symmetry of these two polymorphs[44]. According to Raman group theory, the number of expected Raman-active modes of the ordered spinel ($6A_1+14E+22F_2$) is larger than in the disordered spinel ($A_{1g}+E_g+3F_{2g}$). The Raman spectrum of the LMNO thin film (Figure 1b) shows 6 main components at 160, 404, 499, 525, 597 and 635 cm^{-1} typical of the Raman fingerprint of disordered $LiMn_{1.5}Ni_{0.5}O_4$[45]. This result is in good accordance with a previous study reporting the deposition of the disordered form of LMNO when using working pressure of 0.025 mbar[14]. The X-ray diffraction pattern of the pristine thin film deposited on $Si/Al_2O_3/Pt$ substrate (see Figure S1) displays the typical *hkl* reflections of

Fd-3m spinel LMNO (cubic lattice parameter of 8.16 Å). The two additional peaks labelled by stars at 40° and 46°correspond to the Pt reflections of the current collector.

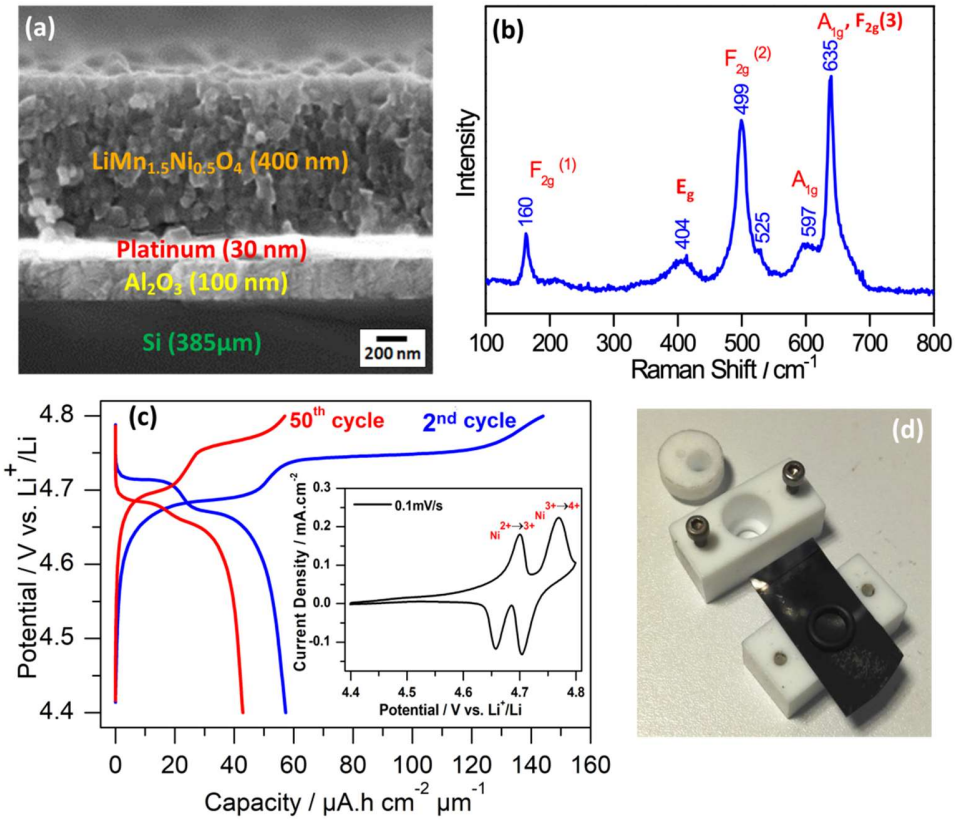

Figure 1. Structural and electrochemical characterization of the pristine LMNO thin film. (a) SEM image of cross section of the LMNO/Si/Al_2O_3/Pt stacking after annealing at 700°C during 2h in air. (b) Raman spectrum of the LMNO thin film. (c) 2nd and 50th charge-discharge cycles of the LMNO thin film recorded at 1C rate (147 $mA.g^{-1}$) in a conventional electrochemical flat cell. In insert: cyclic voltammetric curves recorded at 0.1 mV/s. (d) Electrochemical flat cell used for electrochemical cycling of LMNO thin film. 1M $LiClO_4$ EC:DMC 1:1 electrolyte.

Previous study of the electrochemical properties of sputtered LMNO thin films has shown the benefits of cycling in the 4.4 - 4.8 V vs Li+/Li potential range to avoid the occurrence of the Mn redox system below 4.4 V[13]. Indeed, below 4.4 V, the capacity fade is exacerbated in liquid electrolyte due to Mn disproportionation, leading to the formation of Mn^{2+} and Mn^{4+} species and a dissolution phenomenon. Figure S2 shows the first

charge-discharge cycle at 1C rate of the LMNO thin film in a home-made electrochemical flat cell (Figure 1d), using 1M $LiClO_4$ in EC:DMC (1:1) as electrolyte and lithium metal as reference and negative electrode. The presence of two well-defined plateaus at 4.68 V and 4.75 V is typical of the $Ni^{2+/3+}$ and $Ni^{3+/4+}$ redox couples, respectively. A small activity assigned to the $Mn^{3+/4+}$ system is observed at ~ 4.1 V during the first charge (Figure S2a), due to the formation of a few Mn^{3+} species in the thin film to counterbalance the oxygen deficiency induced by the annealing process of the thin films occurring at 700°C. Another potential plateau can be detected at ~ 4.55 V vs Li+/Li only during the first charge, which is attributed to the presence of inactive Li_2MnO_3 secondary phase[46]. The 2nd and 50th galvanostatic charge-discharge plots in the 4.4 V – 4.8 V vs. Li^+/Li potential window are shown in Figure 1c. The presence of two well-defined plateaus unambiguously signs the redox activity of the $Ni^{2+/3+}$ and $Ni^{3+/4+}$ systems, as observed from cyclic voltammetry experiments (see insert of figure 1c) and reported in previous studies on LMNO thin films[14,16]. The volumetric capacity obtained on 2nd discharge, *i.e.* ~ 58 $\mu Ah.cm^{-2}.\mu m^{-1}$, is close to the theoretical one (63 $\mu Ah \cdot cm^{-2} \cdot \mu m^{-1}$). This corresponds to the exchange of ~0.92 F/mole of spinel oxide, in good agreement with the Li content in the LMNO thin film. A far larger volumetric capacity of ~145 $\mu Ah.cm^{-2}.\mu m^{-1}$ is recovered on 2nd charge, *i. e.* 2.5 fold that obtained in discharge. This extra-capacity is usually attributed to electrolyte decomposition occurring above 4.3 V[47,48]. The unwanted oxidation of the liquid electrolyte indeed occurs at high voltage, resulting in the decomposition of organic solvent molecules (DMC and EC) and lithium salt $LiClO_4$, which leads to the formation of a solid electrolyte interphase (SEI)[47]. Various research groups have reported the beneficial effect of various additives and surface coatings to limit this phenomenon and improve the cycling

stability[46,48,50]. In our conditions, an important capacity fade is observed with only 72% of the initial discharge capacity (42 µAh.cm^{-2}.µm^{-1}) recovered after 50 cycles (Figure 1c). However, as reported in a number of studies[46,50], the capacity decay can be effectively mitigated by coating the LMNO thin film with an 3 nm-thick Li_3PO_4 protective layer made by ALD technique[16] (still 55 µAh.cm^{-2}.µm^{-1} recovered after 50 cycles, see Figure S3). Hence, *in situ* liquid electrochemical TEM experiments have been carried out in this work to capture the key changes taking place in the uncoated LMNO thin film cathode, which is responsible for the huge capacity fade observed upon cycling in liquid electrolyte.

FIB lamella fabrication and connection to the micro-chip

To study thin film cathode in liquid electrochemical TEM cell, it is necessary first, to prepare a thin sample below to 150 nm so that electron beam can pass through it, and second, to transfer and connect the specimen to a micro-chip allowing the electrochemical study in a liquid medium. A focused ion beam (FIB) based approach is commonly used to perform cross section as discussed by Vasile *et al*.[49] and does not require any pretreatment of the samples which makes it more advantageous over the other existing conventional techniques such as ion milling and ultramicrotomy techniques. FIB processed cross section for all-solid-state samples is also used in other works by Wang *et al*.[38] and Fawey *et al.*[19,51] to investigate the interface effects while monitoring electrochemical and structural changes with high spatial resolution.

We used here a FIB/SEM instrument to prepare the thin lamella and to contact the current collector of the thin film cathode to the micro-chip electrode. To ensure a good electrical connection between the thin film cathode and the micro-chip, the platinum

current collector thickness has been changed during the fabrication of thin film cathode to reach 630 nm. A deposition of platinum layer (green box) using GIS with gallium ion beam assisted was performed between the micro-chip electrode and the current collector of thin film (figure 2d). Furthermore, a small amount of platinum on the bottom edge of the sample is deposited (blue box) on silicon nitride window to provide an extra mechanical support and further avoid displacement during the operation inside the *in situ* liquid electrochemical TEM device (figure 2c).

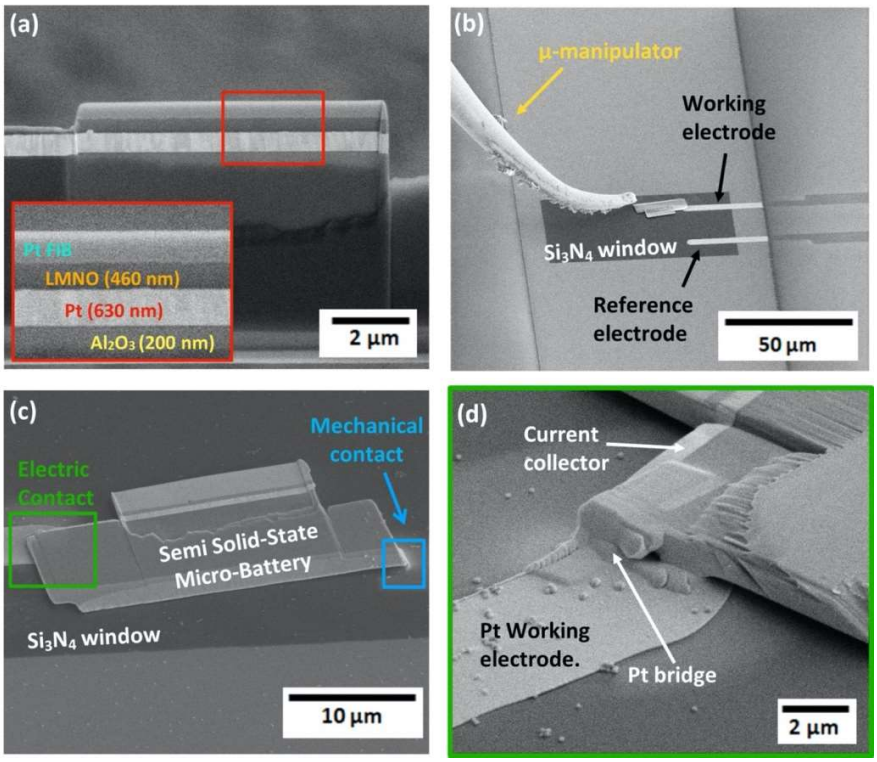

Figure 2: SEM images of the different steps used to transfer a µm thick lamella from the bulk material to electro-contacting micro-chip (Protochips). (a) The bulk thin film with different layers sandwiched on each other, from bottom to top Si/Al_2O_3/Pt-current collector/LMNO/Pt-FIB, insert in red box shows the zoom of the different layers. (b) transfer of the FIB sample with the help of micro-manipulator to the e-chip for the platinum reference electrode of e-chip to platinum current collector of lamella. (c) FIB lamella on the Si_3N_4 window with a Pt deposited on the edge to provide the mechanical support (shown in blue). (d) Formation

of electrical bridge by Pt deposition between the electrical contacts of the micro-chip device and the cathode to enable the electrochemical biasing.

Several studies reported conductivity measurements to characterize nano-scale electrical properties by current-voltage measurement system using multiple-probe Scanning Tunnelling Microscope (STM)[52-54]. There are two purposes of using conductivity test in our work, first is to verify the good contact between the Pt current collector of FIB lamella and the platinum working electrode of micro-chip to prevent the significant polarization during the electrochemical cycles. Secondly, to ensure the highly resistive contact between the platinum protective layer of FIB lamella and the platinum working electrode of the micro-chip to avoid the possibility of leakage current. Figure 3 shows the conductivity measurements recorded between the different platinum layers of FIB lamella sample and the Pt working electrode of the micro-chip. The measurement is performed between the two connected tips, one set at ground and the other one sweeping voltage.

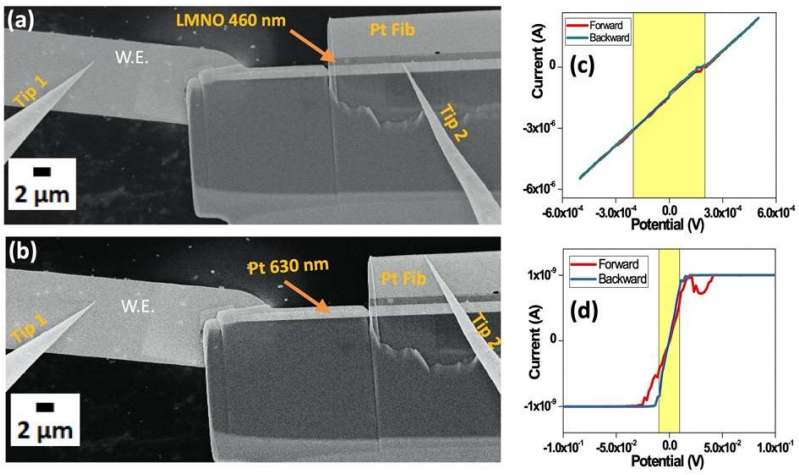

Figure 3. Conductivity measurements inside SEM between the FIB sample and the e-chip, (a) between the platinum working electrode of the e-chip and the platinum current collector of FIB sample, (b) between the platinum working electrode of the e-chip and the platinum protective layer of FIB sample and (c-d) obtained electrical conductivity measurements between different mentioned points.

The conductivity was recorded for 2 distinct measurements. The conductivity values of prepared platinum bridge should be high to ensure the good operation of FIB lamella, thus it is crucial to know the resistivity values of the metal deposited from the gas injection system (GIS) on the micro-chip. The measurement is recorded between the Pt working electrode of the micro-chip and the Pt current collector of micro-battery as shown in figure 3a and the corresponding conductivity graph confirms the high conductive behavior with a resistance of $1.5x10^2$ Ω. It is worth mentioning that the 2-probe measurement also integrates the contact resistance between the probes and the sample, meaning that the real resistance of the bridge may be even lower. Lastly the conductivity measurements result shown in figure 3b, recorded between the micro-chip Pt working electrode and Pt protective layer of FIB as shown in figure 3c confirms the resistive contact between both with high value of resistance ($1.25x10^7$ Ω). Thus, the obtained conductivity results confirm the good quality of FIB preparation and its connection with the micro-chip which makes FIB lamella fit to be cycled inside the electrochemical TEM holder. In the following, we report the study of the FIB lamella sample before and after *in situ* electrochemical cycling to detect the cycled induced differences.

Study of pristine FIB-lamella before cycling

After the successful fabrication of the FIB sample with the careful FIB parameter control, the sample is further installed inside the liquid electrochemical TEM holder. The whole setup of transferring the sample inside the liquid electrochemical TEM holder takes place in a non-controlled environment, with no flow of electrolyte for the initial study of pristine sample. Later, the holder is then placed inside the TEM to get useful analytical

information (figure S6). 4D-STEM ASTAR analysis along with precision electron beam technique is used to obtain the information about micro/local structural and textural relationship, and most importantly the morphological and phase details of the LMNO layer along its electrochemically active part together with the electrolyte before cycling. This type of investigation has been already done for the study of various thin film[55,56]. The study of electrochemical activity in battery by 4D-STEM mapping was first reported by Kübel *et al.*[57] in which the authors showed the statistical orientation information on the $LiFePO_4/FePO_4$ interface in individual grains with phase mapping extracted from ASTAR data. Other similar works based on the mapping of crystalline phase and orientation mapping using 4D-STEM approach is reported by Su *et al.*[58] and Brunet *et al.*[59]

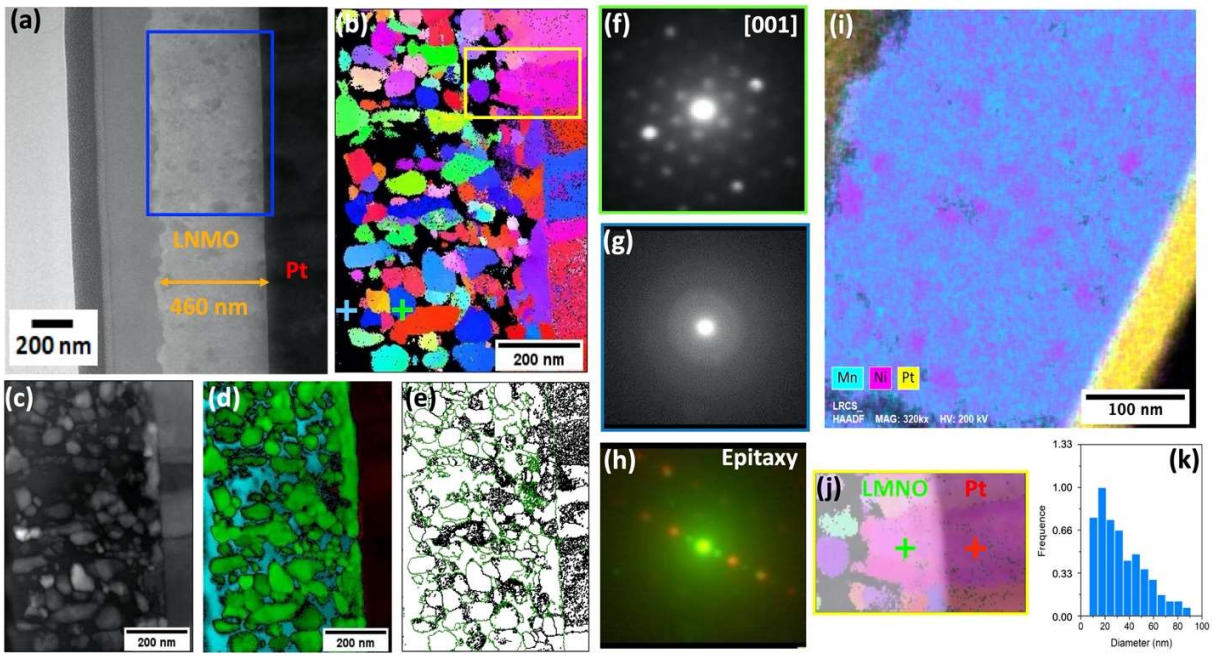

Figure 4: (a) TEM image of the LMNO FIB lamella sample before cycling, (b) orientation map according to the Y axis, (c) index map (d) phase map where black represents the platinum, in green the LMNO phase and in blue the amorphous phase; (e) grain boundaries map, (f-g-h) electron diffraction pattern of spinel LMNO, porosity and combination of platinum and LMNO showing the epitaxial effect between the two phases, (i) EDS mapping showing Si in black, Pt in yellow, pink and blue corresponds to Mn and Ni respectively, (j) epitaxial effect of LMNO on Platinum (k) Grain size distribution map of the analyzed area.

The cross-section bright field TEM image of a pristine lamella is shown in figure 4a. All layers are easily identified by contrast: Si substrate, Al_2O_3, Pt, LMNO thin film and Pt protective coating. At high magnification, the distinction between all the stacked layers is remarkable and the thickness of the LMNO is found to be 460 nm (highlighted in yellow). It is worth noticing that the layer sequence established through bright field TEM image was confirmed through EDX-STEM chemical mapping analysis of the cross section (figure 4i: Si black, Pt yellow, Mn turquoise blue, Ni pink). The chemical composition of each layer is indeed nicely monitored. Moreover, both bright field image and EDX analysis give evidence that the layers interfaces are well defined without inter-diffusion phenomena during the FIB preparation process, thus proving the relevance of our deposition procedure for the stacking layers. In addition, no further gallium implantation is involved during the cutting process. Furthermore, homogeneous distribution of Mn and Ni is found within the LMNO layer, with slightly brighter nickel regions than manganese ones, confirming the presence of more Ni-rich and less Mn-rich impurities in the LMNO layer, which is in agreement with results reported for the disordered LMNO powder[60]. In the homogeneous areas, the EDX analysis indicates a Mn:Ni ratio close to 1:0.3, which is consistent with $LiMn_{1.5}Ni_{0.5}O_4$ composition (figure S7a).

Next, the structure and morphology of LMNO crystallites inside the thin layer is analyzed using electron diffraction in parallel beam condition. Figure 4b shows 4D-STEM-ASTAR map of the selected region (blue box in figure 4a) in the pristine LMNO layer with a scan-step of 2 nm (spatial resolution). While the overall particle orientation seems to be random, each of the particles inside the LMNO layers exhibit specific crystallographic

orientation that are represented by adopting the color code routine. The 4D-STEM recorded at different regions of selected area in LMNO layer is shown in figure 4, where figures 4f-g-h represent the electron diffraction patterns recorded on the LMNO grain (green plus sign in figure 4b) aligned along [001] orientation and the black region representing amorphous/porosity (blue plus sign in figure 4b) respectively. It was previously reported that the working pressure used to deposit LMNO (0.025 mbar) will bring 20% porosity in the sample[14]. Orientation mapping in figure 4b shows more blue color grains, which means that all those grains are aligned around the [001] orientation. A statistical analysis of the grain orientation is computed to obtain the polar figure in which [001] orientation is a maximum. In accord with orientation relationship between the neighboring grains, a grain boundary is shown in figure 4e (in green) where quite several grains are observed with a typically well-defined boundary between different orientations. However, unconnected grains are also observed inside the layer, which must be inactive during the electrochemical reaction.

The sputtering deposition process was achieved at a working pressure of 0.025 mbar that allows depositing the nanometric LMNO grain-sized on the Pt surface. From 4D STEM-ASTAR analysis, the grain size distribution can be extracted (figure 4k), where the mode value of the grain size found in the LMNO layer is nearly 20 nm, with most of the grains of size ranging between 10-40 nm. Further, phase map processed with the 4D STEM-ASTAR (Figure 4d) shows the Pt layer (black), disordered LMNO phase (green) and porosity/amorphous (turquoise blue) where the contribution of each phase is found to be 18%, 57% and 25% respectively. The calculated porosity by mapping in the FIB lamella sample, with a value around 20%, well confirms that of the reported during the

preparation of thin film[13]. The black color represents the region where the phases are found to be amorphous (figure 4g). This can correspond to either porosity with Si_3N_4 membrane response or amorphous phase. Moreover, a (111) preferred orientation is observed along the 20 nm thick Pt layer (pink color). The enhanced view of the region highlighted in yellow (Figure 4b) is shown in Figure 4j**,** where the same color code is observed by 4D STEM-ASTAR study for both LMNO (marked in green) and Pt (marked in red) grains exhibiting the same [111] orientation, thus validating the epitaxial relationship between the two layers. This is supported by the diffraction pattern shown in figure 4(h), recorded on LMNO grains (marked in green) and Pt (marked in red). Both diffraction patterns were found to be completely superimposed to each other, further justifying the epitaxial growth effect of LMNO grains on the Pt current collector, which has been observed in different interface areas of the FIB lamella sample. Letiche *et al*.[13] and Hallot *et al*[16] have confirmed the presence of epitaxial effect in such thin film preparation process and reported the use of X-ray diffraction pole figure analysis to discriminate between the epitaxial and fiber texture behavior. In their study, they have claimed the role of the pressure deposition being responsible for the changes in the preferential orientation of the LMNO film on Pt current collector. These epitaxial interfaces between active materials and current collector randomly distributed in the lamella could induce heterogenous effect during the electrochemical cycling.

In situ TEM study of the cycled FIB-lamella

After the study of pristine FIB lamella by different TEM techniques such as 4D STEM-ASTAR, EDX and TEM imaging before electrochemical cycling, several cycles of

cyclic voltammetry (CV) were recorded inside the electrochemical TEM device, keeping the electron beam off to avoid electron beam damage on $LiMn_{1.5}Ni_{0.5}O_4$ layer. The Figure 5a-b shows the schematic description of the Poseidon Select TEM holder used for electrochemical measurements in liquid electrolyte. The micro-chip used for TEM study is shown in figure 5c with the three Pt electrodes (reference, working and counter), out of which reference and working electrodes are observed from the Si_3N_4 window that is transparent to electron beam (insert image in Figure 5c). The TEM image in figure 5d shows the connection between the FIB lamella sample and the e-chip. Hence, we started with an electrochemically active sample with Pt as a current collector for the LMNO positive electrode connected with the Pt working electrode of micro-chip, which was further sandwiched inside the holder tip of the electrochemical TEM cell. *in situ* TEM cell was assembled using an electrolyte made of 1M $LiClO_4$ dissolved in equal ratio of EC (ethylene carbonate) and DMC (dimethyl carbonate). To establish its electrochemical performance, cyclic voltammetry was applied using a sweep rate of 0.1 $mV.s^{-1}$ using Pt as counter and pseudo-reference electrodes. Microfluidic controller is used to control the flow of electrolyte inside the electrochemical TEM holder. The flow rate is 5 $\mu L.min^{-1}$. The complete setup of electrochemical TEM holder (inserted inside the TEM instrument) and its connection with potentiostat (Biologic SP200) and microfluidic controller is shown in figure S6a-b. The use of disordered LMNO as a positive electrode material provides higher Li ion mobility, mostly due to the presence of 3D Li diffusion pathways in the cubic lattice. Further, Kunduraci *et al.*[61] shows the electronic conductivity of disordered LMNO is 2.5 order of magnitude higher than ordered LMNO, which is explained by the higher electron conduction between mixed $Mn^{3+/4+}$ cations compared with pure Mn^{4+}. As

discussed above, the measured bulk density was estimated to be around 80% of the theoretical value (20% porosity in the thin film sample). The following two main conclusions can be drawn from the above discussed points: (i) the open spaces/porosity between the LMNO layer allows for enhanced diffusion of electrolyte and more efficient utilization of electroactive sites; (ii) the binder-free feature not only leads to improved conductivity, but effectively avoids agglomeration of active materials. The electrochemical Impedance Spectroscopy (EIS) analyses (figure 5e) recorded at open circuit voltage, shows 2 semi circles at very high (2360 Hz) and medium (35 Hz) frequencies. The equivalent circuit for the obtained impedance profile is shown in figure S8a. The equivalent circuit consists of three parts to represent the physical and electrochemical processes in the system. The combination of constant phase element (CPE_1) and a resistance (R_1) connected in parallel describe the battery behavior at high frequency. The middle-frequency region is modeled by CPE_2 and R_2 connected in parallel. In the low frequency region (3.0-0.5 Hz), another CPE_3 instead of a Warburg impedance is used to describe the diffusion characterization. These potential controlled electrochemical impedance spectroscopy (PEIS) measurements quantify the global resistance of the setup with a relatively high resistance value (around $1x10^6$ Ω), which can be associated to the summation of multiple interfaces present in the system such as holder/potentiostat, micro-chip/holder, FIB lamella/micro-chip and LMNO layer/Pt current collector.

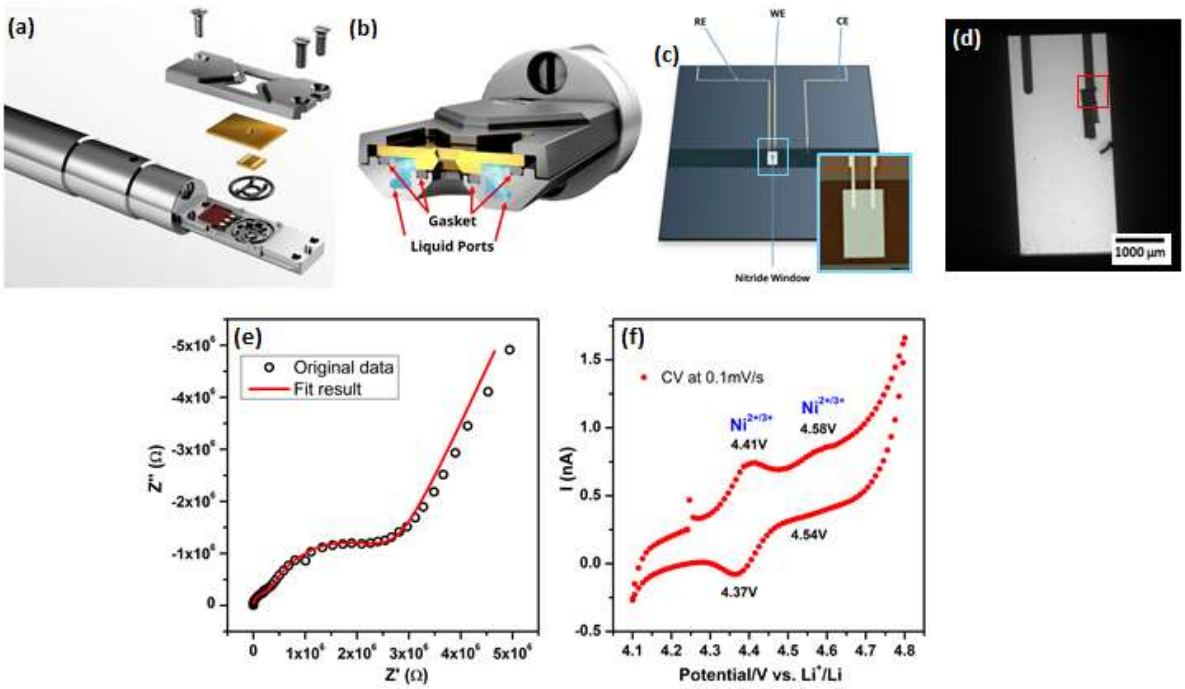

Figure 5: Electrochemical study of FIB-lamella inside the electrochemical TEM holder (a) Schematic description of the Poseidon Select TEM holder (Protochips) for operando electrochemical measurements; (b) exploded view showing the holder tip with precision slot for loading liquid cell where O-ring gasket is used to get a good vacuum-sealing; (c) the top e-chip containing a printed reference (platinum), counter (platinum), and working electrode (platinum). (d) TEM image showing the connection between the platinum current collector of FIB sample with the platinum working electrode of e-chip; (e) fitted nyquist plot showing the global impedance of the system; (f) Cyclic voltammogram measured in a holder with a voltage sweep rate of 0.1 mV/s in the potential window of 4.1 V-4.8 V using 1M $LiClO_4$ EC:DMC 1:1 electrolyte.

Figure 5f shows the cyclic voltammetry curves for the TEM holder recorded in the potential range of 4.1 and 4.8 V vs. Li^+/Li. Two well defined peaks are observed at 4.41 V and 4.58 V corresponding to $Ni^{2+/3+}$ and $Ni^{3+/4+}$redox couple, indicating the change of the oxidation state of Ni during charging above 4.4 V. The use of Pt pseudo reference is at the origin of small shifts in the potentials measured (~200 mV). Another noticeable point is the deformation of the CV curve following an inclined line, which is consistent with the present of a high internal resistance as previously showed by PEIS analysis. It is worth noticing that no Li metal is used as counter electrode, our *in situ* system is therefore similar to an anode-free electrochemical system. In addition, a huge amount of electrolyte

oxidation is observed above 4.6 V, which is normal at a high potential (electrolyte is unstable above 4.3 V) and could also influence the deformed CV curve above 4.3 V.

Study of the LMNO thin film after electrochemical cycling

After the liquid electrolyte draining and washing th FIB lamella several times with DMC, the cycled LMNO thin film is characterized to quantify the degradation and damage induced by (de)lithiation process. The low-resolution STEM images of the cycled thin film (Figure 6) shows the LMNO layer and its intersection with the Pt layer exhibit a white High-angle annular dark-field imaging (HAADF) contrast.

In figure 6a, an accumulation of organic compounds (white cloud) denoted by white arrows can be spotted in the LMNO layer. Such an undesirable products, which appear during the cycling, was due to the electrolyte decomposition and continuous electrode-electrolyte reaction that happens for such high operating voltage materials[62]. Although, $LiClO_4$ has been a popular electrolyte solute owning to its high solubility, high conductivity and has also the merits of being relatively less hygroscopic and is stable at ambient temperature. However, the high oxidation state of chlorine (VII) in perchlorates makes it a strong oxidant that reacts with the most organic species and reacts even more violently with the positive electrode material at high operating voltage[63]. The products of decomposition of lithium perchlorate could be represented by the equation: $LiClO_4$ -> LiCl + $2O_2$ and decomposition products result in loss of electrolyte during operation. Detailed work by Yang *et al*.[64] identify undesirable products formed when the electrode material comes in contact with the EC solvent. The EDX analysis of the cycled LMNO layer is shown in supplementary figure S8 where Cl peak are observed corresponding to possible organic decomposition products.

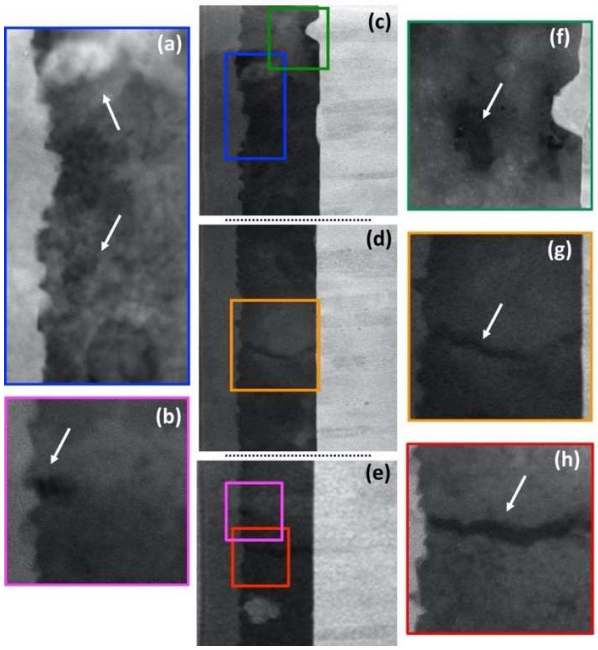

Figure 6: STEM image of the cycled induced differences in the LMNO thin film. (a and c) Accumulation of organic compounds denoted by white arrows inside the LMNO layer observed after cycling, (b, c, e and f) formation of voids in the LMNO layer after cycling denoted by white arrows, (d, g and h) formation of cracks inside the LMNO layer after cycling denoted by white arrows.

From STEM images, we also note the presence of cracks inside the LMNO layer (Figure 6d-e highlighted in orange and red boxes and enlarged view in Figure 6 g-h). The formation of these cracks could have two origins: (i) lithium diffusion-induced stress, especially within a layer containing high density of grain boundary and (ii) volume change of 6.4% between the lithiated and delithiated states. Along with the cracks, several voids are also observed after the electrochemical cycling (Figure 6 b-f). The cause of the voids formation is reported in the case of cobalt free electrode materials, especially at high voltage (> 4.5 V), due to dissolution of the transition metal in the electrolyte with the cycling which is also the responsible for poor cycle life[65]. We also observe the loss of contact between the LMNO layer and the Pt current collector due to the low adhesion strength at this interface (**Figure 6b**). The adhesion strength plays a critical role in cycling

durability of electrode materials and low adhesion strength between the thin film and substrate makes active materials failing, thus resulting in poor stability. In addition, the nanometric size of the LMNO particles effectively alleviates the occurrence of large stress which can also result in the loss of contact between the layers.

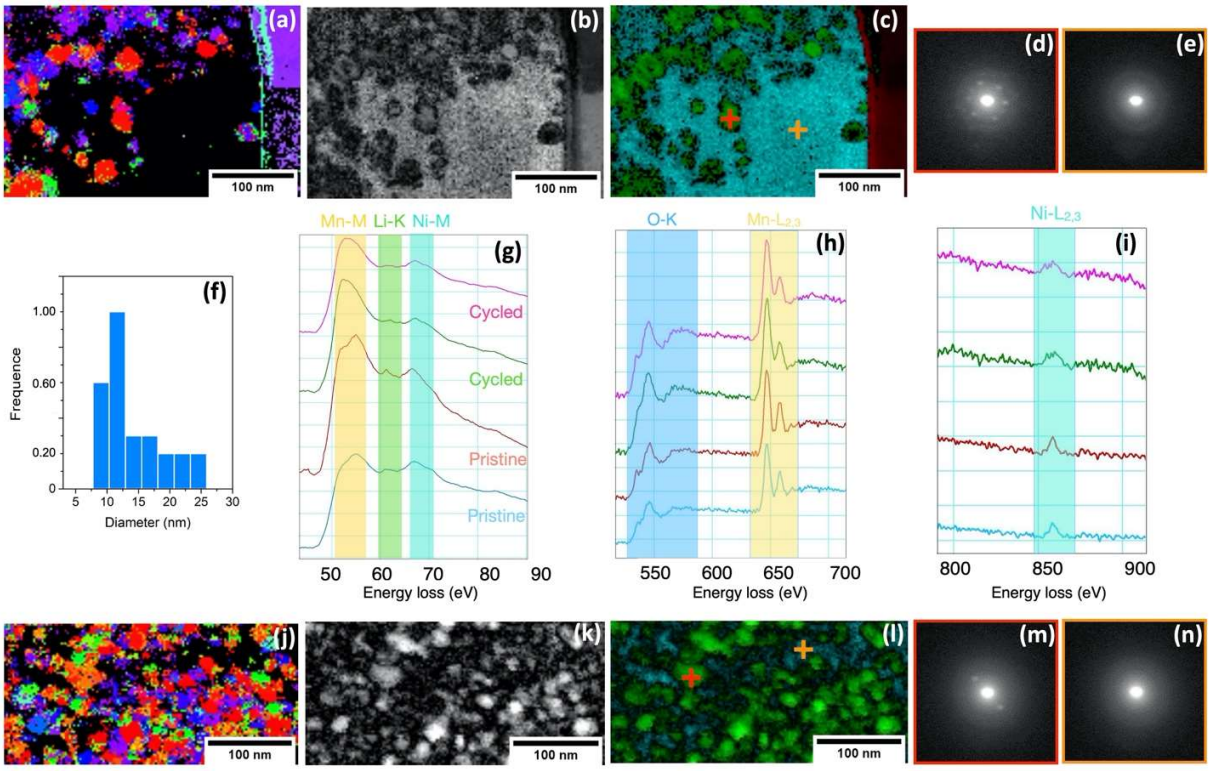

Figure 7: 4D-STEM-ASTAR and EELS spectroscopy analyses of LMNO thin film cycled inside TEM for two different regions of interest. (a,j) Crystalline orientation map (b,k) phase reliability map (in black represented the areas where the indexation has a low reliability). (c, l) phase map (disordered LMNO phase) where in green the LMNO phase and in blue the amorphous phase. (d,m) electrons diffraction pattern of LMNO crystals. (e,n) electrons diffraction pattern of amorphous phase. (f) Grain size distribution extract from these two ROI. (g-i) EELS spectrum of 2 areas before and after electrochemical cycling, (g) in low loss region (Mn-$M_{2,3}$, Li-K and Ni-$M_{2,3}$ edges) and (h,i) in core loss region (O-K, Mn-$L_{2,3}$ and Ni-$L_{2,3}$ edges).

Figure 7a-j shows orientation maps from 4D STEM-ASTAR analyses of two regions in the cycled LMNO thin film. Comparing the grain size distribution (figure 7f) to that of the pristine thin film where the average diameter was quantified to 20 nm, the value decreases to 10 nm after cycling. Furthermore, the amorphous parts in the layer are more predominant than initially observed in the pristine thin film, especially in Figure 7c where almost half of the surface area is amorphous (see diffraction pattern in Figures 7e-m). In figure 7l less amorphous regions are observed but the average LMNO grain size undergoes a drastic modification. Based on the diffraction patterns of smaller LMNO Grains (figures 7d-m), the Bragg spots seem to be less intense, meaning that the crystallinity of grains is less pronounced.

These *in situ* observations are consistent with the analysis made on FIB lamella of disordered LMNO pristine and *ex situ* cycled with identical cycling conditions (see figure S09, S10 and S11). Figure S10 and S11 shows 4D STEM-ASTAR analyses of *ex situ* cycled sample (cycled using flat electrochemical cell) in which the grain size reduction and amorphous phase are also clearly identified. The convergence between *in situ* and *ex situ* results reinforce our conclusions on the structural modifications occurring during the electrochemical cycling. The appearance of amorphous phase and grain size modification could be associated to manganese migration occurring at high voltage with a high surface/volume ratio sample, in which the oxidation of liquid electrolyte is enhanced. EELS spectroscopy analyses of these areas before and after the *in situ* electrochemical cycling shown in figure 7g exhibit the low loss region in which Mn $M_{2,3}$-edge, Li K-edge and Ni $M_{2,3}$-edge are identified. A slight decrease of Li peak intensity is observed in comparison with those of pristine FIB lamella suggests that less lithium is

present inside LMNO structure after *in situ* electrochemical cycling. The $M_{2,3}$-edge of Mn is clearly modified between cycled and pristine with a lower energy shift, which can be associated to the reduction of LMNO particle size and the increase of surface/bulk ratio[66,67]. Regarding the core loss zone for EELS spectra, O K-edge and Mn $L_{2,3}$-edge present no clear modification between cycled and pristine, especially for the Mn L_3/L_2 ratios indicating no change in the valence state of Mn cations (estimated between $^{3+}$ and $^{4+}$). On the contrary, the Ni $L_{2,3}$-edge is modified after cycling as shown in figure 7h. This is consistent with low loss EELS analysis and confirm that the delithiation process occurred in the micro-battery during the TEM *in situ* experiment. In LMNO thin film, further EELS spectroscopy investigations with high spatial resolution are needed to have an accurate identification and quantification of oxidation state modification in specific areas. The correlation to electron diffraction mapping would rise our understanding of electrochemical phenomena that transform the LMNO structure in the surface and the bulk and cause the capacity fading.

Conclusion

The focused ion beam technique was successfully used to obtain thin cross-sectioned microbattery sample out of a semi solid state micro-battery. The good electrical contact between the platinum working electrode of the micro-chip and the platinum current collector of FIB lamella sample was measured by multiple-probe STM with nanoscale precision. Furthermore, a thickness of ~20nm along the platinum layer, a (111) preferred orientation is observed exhibiting the epitaxial effect of LMNO on Pt layer which has been further supported by the 4D-STEM ASTAR recorded on both LMNO and

platinum grains. The FIB lamella sample was then studied by *in situ* TEM to determine the source for defect in assembled batteries and the capacity fade phenomena observed for uncoated LMNO thin films cycled in conventional liquid electrolyte. The cyclic voltammetry curve analysis of the FIB lamella was made possible thanks to an electrochemical TEM holder that allows the controlled flow of electrolyte (5µL/min). The comparison between the pristine and cycled FIB lamella LMNO observed by TEM allowed us to clearly demonstrate the formation of cracks inside the LMNO layer, loss of contact between the LMNO layer and the Pt current collector as well as the agglomeration of organic compounds products due to the electrolyte decomposition. Moreover, 4D STEM-ASTAR technique provided us crucial information regarding the grain size reduction from 20 nm in the pristine to 10 nm in the cycled cathode, confirming the continuous electrode-electrolyte reaction happening upon cycling. In addition, the decrease in crystallinity and increase in the amorphization of the LMNO grains by 38 % in the cycled sample clearly proves the fast capacity fade phenomena observed in liquid electrolyte. EELS analysis confirms the modification of Li K-edge, Mn M-edge and Ni $L_{2,3}$-edge after cycling, as a result of the delithiation process.

Although *in situ* TEM observations have provided key information, it was difficult to present the various states of charge or discharge due to the high reactivity of the positive electrode material with the electrolyte, preventing the system to attain the relaxed state. Our motivation to develop an experimental setup enabling the cycle of the thin film cathode inside TEM column while performing the *in situ* observation was challenging due to the optimization of multiple technical points and to the use of liquid electrolyte for electrochemical cycling. However, this study is the first reporting the TEM study of a thin

film cathode cycled in liquid electrolyte inside the TEM and important observation solely needed for the control and improvement of a Lithium based micro-battery assembly are reported. Indeed, TEM observation is one of the fundamental techniques leading to a fast development of commercial 2D and 3D all-solid-state micro-batteries to power miniaturized sensors for IoT applications. The quality of cyclic voltammetry curve for a such difficult electrochemical conditions is markable. Further work will involve the electrochemical cycle of FIB prepared lamella from a full all-solid-state micro-battery in the *in situ* TEM cell to monitor in real-time the structural and morphological modifications in electrode materials during electrochemical cycling.

Methods.

Thin film preparation. The thin film preparation is well explained by Hallot *et al.*[14] which consists of an Al_2O_3 layer, which acts as a diffusion barrier[13] (thickness = 100 nm) is deposited on a [100] oriented silicon wafer (diameter = 7.6 cm) by Atomic Layer Deposition (ALD) in a PicoSun R200 reactor. A Plassys MEB 550S equipment is used to evaporate the 630 nm-thick platinum on the aluminum oxide layer. While a Radio Frequency magnetron sputtering is used to deposit $LiMn_{1.5}Ni_{0.5}O_4$ (hereafter LMNO) electrode, under Argon atmosphere, in a CT-200 cluster from Alliance Concept using a pure $LiMn_{1.5}Ni_{0.5}O_4$ target (99.999%, 10 cm diameter and 6 mm thick) at the pressure of 0.025 mbar. The CT-200 equipment is pumped to 10^{-6} mbar, before preparing for the sputtering deposition. The deposition is achieved at room temperature while fixing the distance between the target and the substrate holder to 60 mm. The power used to bias the target is fixed to 100 W (1.27 $W.cm^{-2}$). A Bernstead International F600 Furnace with

a heating/cooling ramp (dwell) of 5 °C.min^{-1} is used for two hours at 700 °C for the annealing of as deposited stacked layers (Al_2O_3 / Pt / $LiMn_{1.5}Ni_{0.5}O_4$) under air. The thickness of the LMNO layer is measured close to 460 nm. This as-prepared semi all solid battery is used to perform bulk electrochemical study (Shown in figure 1(a)).

Morphological analysis and structural characterization of thin film. The thickness and microstructure of the films are determined using a scanning electron microscope (SEM Zeiss supra55-VP). A Rigaku SMARTLAB multipurpose six-axis diffractometer (9 kW rotating an- ode) using Cu-Kα radiation (λ = 1.5418 Å) and a LaBRAM HR 800 (Jobin-Yvon-Horiba) Raman spectrometer with a He:Ne laser 632.8 nm as an excitation source are used to identify the structure type of the bulk film (ordered / disordered phase), respectively.

Electrolyte preparation. Lithium perchlorate salt ($LiClO_4$, anhydrous, 99%), Ethylene carbonate ($C_3H_4O_3$, anhydrous, 99%) and Dimethyl carbonate ($C_3H_6O_3$, anhydrous, 99%) were purchased from Alfa-Aesar. The 1M $LiClO_4$ EC: DMC 1:1 was prepared in an argon-filled glovebox (0.1 ppm of O_2/0.1 ppm of H_2O). The water content of the electrolyte solutions was analyzed by Karl Fischer titration and was found to be below 20 ppm.

Cyclic Voltammetry and Galvanostatic cycling of bulk thin film. Cyclic voltammetry (CV) and galvanostatic charge and discharge plots were investigated on the VMP3 potentiostat/galvanostat equipment using homemade Teflon like flat cell with Li metal used as the counter and reference electrode. The electrolyte (1 mL), comprising 1M $LiClO_4$, dissolved in ethylene carbonate (EC) and dimethyle carbonate (DMC) in a 1:1 ratio, was poured into the flat-cell cavity. The tested area (circular shape) of the sample

was limited to 0.785 cm^2. The flat cells under test were placed in a glove box with controlled atmosphere (O2 and H_2O quantities: less than 1 ppm).

***Preparation of FIB lamellar sample*.** Focused Ion Beam (FIB) cross-sectional lamella are prepared using a FEI STRATA DB 235 microscope. Milling steps was performed at 30 kV with current decreasing from 20 nA to 30 pA while lamella thickness decreasing from 6 µm down to 100 nm, followed by a final step at 5 kV and 30 pA to minimize amorphization. Lamella transfer from sample to TEM grid is obtained by Kleindiek micromanipulator.

Multiple-probe conductivity measurement. The test is performed on the system called nanoprobe (Omicron Nanotechnology GmbH) which is installed at IEMN[68] (CNRS, France) where the attention has been given to precisely control the STM tips that are bought in contact with the different FIB-lamellar layers. The whole system is operated in Ultra-High Vacuum (UHV) and it can be described in three important parts: (i) a Scanning electron microscope (SEM, UHV-Carl Zeiss Gemini) with a resolution in the order of 5nm and images acquired from the top of the sample and probes; (ii) a multiple-probe Scanning Tunneling Microscope (STM) whith4 independent STM scanners for imaging, contact and manipulation of nanostructures under SEM monitoring. Two of these STM probes were used to measure the conductivity between different platinum layers of FIB lamella sample and the platinum working electrode of e-chip. (iii) The third part is the control system which is the key component required to operate the system. It combines SPECS-Zürich Nanonis STM controllers to operate the STM probes at the nanoscale with Keithley Source-Measure Units (SMU) to perform transport measurements.

In situ Electrochemical (S)TEM Experiments. FEI-TECNAI G2 (S)TEM equipped with a Schottky field-emission gun and a fast camera Oneview-Gatan (30 fps at 4k) is used for *in situ* TEM experiments. During these experiments, the microscope was operational at 200 kV in both HAADF-STEM and conventional TEM modes. In this study, we checked the effect of the electron beam used to make the observations in TEM and STEM modes to be sure that the beam does not have any effect on our results. To limit typical beam damage effects (bubble and precipitate formations), due to the degradation of the electrolyte by radiolysis effect, the dose was kept below 10 e^-/nm^2 s, during the observations. Protochips Poseidon Select consisting of a microfluidic flow system and an electrochemical measurement system with three electrodes is used as a TEM holder. Where, the holder tip, contains the FIB lamella cell and two silicon e-chips sealed by Viton O-ring gasket, a top micro-chip with three Pt electrodes (reference, counter and working) with 500 nm SU-8 polymer spacer and a 50 nm thick Si_3N_4 window and another is bottom micro-chip (with a 5 µm spacer and a 50 nm thick Si_3N_4 window). To ensure a good vacuum sealing, mounted E-chips are then compressed onto O-rings using screwed lid of the holder. The microfluidic system which is integrated in the TEM holder is used to introduce flow of the electrolyte with a rate range from 0.5 to 5 µL/min using a syringe pump system. Prior to *in situ* experiment, argon gas is used to flush the microfluidic system (cell and micro tubes) to discard oxygen presence.

For 4DSTEM-ASTAR study, the images were generated by plotting the intensity of the transmitted electron beam in the series of acquisition. To eliminate the points with low reliability, intensity is fixed to minimum of 52. A region of interest of 1.2 μm^2 was chosen for the scanning area with a step size of 2.5 nm. To reduce the dynamical effects

and increase the quality of the electron diffraction pattern a precession semi-angle of 0.7° was used.

Cyclic Voltammetry and Electrochemical Impedance Spectroscopy of FIB-lamella connected on e-chip. Cyclic voltammetry and electrochemical impedance spectroscopy were conducted using an ultra-low current SP-200 Biologic potentiostat, where the CV was performed at a sweeping rate of 0.1 $mV.s^{-1}$ between 0.3 V and 1 V using platinum as pseudo reference electrode and Platinum as counter electrode with 1M $LiClO_4$ EC:DMC 1:1 electrolyte. For the sake of precision, all values were then rescaled versus Li^+/Li to yield a potential window of 4.1 V and 4.8 V (vs. Li^+/Li). Impedance measurement was performed in the frequency range 4×10^4 to 0.5×10^{-3} Hz. The excitation signal was 10 mV peak to peak.

ASSOCIATED CONTENT

Supporting Information

AUTHORS INFORMATION

Corresponding Author

*E-mail: (A.D.) arnaud.demortiere@energie-rs2e.com

Author Contributions

A.D. designed the *in situ* TEM experiment. M.H. and C.L. prepared the stacked thin films A.B., P.R., J.P.P.R., R.B.H. perform the characterizations of bulk 2D thin film. A.B. performed the electrochemistry of the bulk thin film. D.T. performed the FIB lamella preparation. M.B. performed the conductivity test. A.B., N.F. and A.D. performed the *in*

situ TEM measurements and analyses. S.C., N.F. and AD performed and analyzed 4D-STEM ASTAR measurements. A.B. and A.D. wrote the manuscript that all authors edited.

Notes

The authors declare no competing financial interest.

ACKNOWLEDGEMENTS

The authors acknowledge the French ANR project “CASSIOPES” N°17-CE09-0016-03 for PhD financial support. The authors also want to thank the French network on electrochemical energy storage (RS2E) and the Store-Ex Labex for the support. The French RENATECH network and the University of Lille are greatly acknowledged for the supporting the Center of MicroNanoFabrication (CMNF) facility. Chevreul Institute (FR 2638), Ministère de l’Enseignement Supérieur et de la Recherche, Région Hauts de France and FEDER are acknowledged for supporting and funding XRD facilities. The authors would like to thank Dr. Kirill Cherednichenko, Dr. Muriel Veron and Dr. Edgar Rauch for the fruitful discussions on the ASTAR experiments.

REFERENCES

(1) Tarascon, J. M.; Armand, M. Issues and Challenges Facing Rechargeable Lithium Batteries. *Nature*. November 15, 2001, pp 359–367. https://doi.org/10.1038/35104644.

(2) Mauger; Julien; Paolella; Armand; Zaghib. Building Better Batteries in the Solid State: A Review. *Materials (Basel).* **2019**, *12* (23), 3892. https://doi.org/10.3390/ma12233892.

(3) Chen, R.; Qu, W.; Guo, X.; Li, L.; Wu, F. The Pursuit of Solid-State Electrolytes for Lithium Batteries: From Comprehensive Insight to Emerging Horizons. *Materials Horizons*. Royal Society of Chemistry November 1, 2016, pp 487–516. https://doi.org/10.1039/C6MH00218H.

(4) Suzuki, A.; Sasaki, S.; Jimbo, T. Development of All-Solid-State Thin-Film Secondary Battery for MEMS and IoT Device. In *Journal of Physics: Conference Series*; Institute of Physics Publishing, 2019; Vol. 1407. https://doi.org/10.1088/1742-6596/1407/1/012037.

(5) Ellis, B. L.; Lee, K. T.; Nazar, L. F. Positive Electrode Materials for Li-Ion and Li-Batteries. *Chemistry of Materials*. American Chemical Society February 9, 2010, pp 691–714. https://doi.org/10.1021/cm902696j.

(6) Xia, H.; Wan, Y.; Assenmacher, W.; Mader, W.; Yuan, G.; Lu, L. Facile Synthesis of Chain-like LiCoO2 Nanowire Arrays as Three-Dimensional Cathode for Microbatteries. *NPG Asia Mater.* **2014**, *6* (9), e126. https://doi.org/10.1038/am.2014.72.

(7) Baddour-Hadjean, R.; Golabkan, V.; Pereira-Ramos, J. P.; Mantoux, A.; Lincot, D. A Raman Study of the Lithium Insertion Process in Vanadium Pentoxide Thin Films Deposited by Atomic Layer Deposition. *J. Raman Spectrosc.* **2002**, *33* (8), 631–638. https://doi.org/10.1002/jrs.893.

(8) Baddour-Hadjean, R.; Pereira-Ramos, J. P.; Navone, C.; Smirnov, M. Raman Microspectrometry Study of Electrochemical Lithium Intercalation into Sputtered Crystalline V2O5 Thin Films. *Chem. Mater.* **2008**, *20* (5), 1916–1923. https://doi.org/10.1021/cm702979k.

(9) Needle-like LiFePO4 thin films prepared by an off-axis pulsed laser deposition technique - [PDF Document] https://fdocuments.in/document/needle-like-lifepo4-thin-films-prepared-by-an-off-axis-pulsed-laser-deposition.html (accessed May 5, 2020).

(10) Yim, H.; Shin, D. W.; Choi, J. W. LiMn2O4-Based Cathode Thin Films for Li Thin-Film Batteries. *J. Korean Phys. Soc.* **2016**, *68* (1), 41–53. https://doi.org/10.3938/jkps.68.41.

(11) Jilani, A.; Abdel-wahab, M. S.; Hammad, A. H. Advance Deposition Techniques for Thin Film and Coating. In *Modern Technologies for Creating the Thin-film Systems and Coatings*; InTech, 2017. https://doi.org/10.5772/65702.

(12) Manthiram, A.; Chemelewski, K.; Lee, E. S. A Perspective on the High-Voltage LiMn1.5Ni0.5O 4 Spinel Cathode for Lithium-Ion Batteries. In *Energy and Environmental Science*; Royal Society of Chemistry, 2014; Vol. 7, pp 1339–1350. https://doi.org/10.1039/c3ee42981d.

(13) Létiche, M.; Hallot, M.; Huvé, M.; Brousse, T.; Roussel, P.; Lethien, C. Tuning the Cation Ordering with the Deposition Pressure in Sputtered LiMn1.5Ni0.5O4 Thin Film Deposited on Functional Current Collectors for Li-Ion Microbattery Applications. *Chem. Mater.* **2017**, *29* (14), 6044–6057. https://doi.org/10.1021/acs.chemmater.7b01921.

(14) Hallot, M.; Demortière, A.; Roussel, P.; Lethien, C. Sputtered LiMn1.5Ni0.5O4 Thin Films for Li-Ion Micro-Batteries with High Energy and Rate Capabilities. *Energy Storage Mater.* **2018**, *15*, 396–406. https://doi.org/10.1016/j.ensm.2018.08.012.

(15) Kim, J.-H.; Myung, S.-T.; S. Yoon, C.; G. Kang, S.; Sun, Y.-K. Comparative Study of LiNi0.5Mn1.5O4-δ and LiNi0.5Mn1.5O4 Cathodes Having Two Crystallographic Structures: $Fd\bar{3}m$ and P4332. *Chem. Mater.* **2004**, *16* (5), 906–914. https://doi.org/10.1021/cm035050s.

(16) Hallot, M.; Caja-Munoz, B.; Leviel, C.; Lebedev, O. I.; Retoux, R.; Avila, J.; Roussel, P.; Asensio, M. C.; Lethien, Ch. Atomic Layer Deposition of a Nanometer-Thick Li_3PO_4 Protective Layer on $LiNi_{0.5}Mn_{1.5}O_4$ Films: Dream or Reality for Long-Term Cycling? *ACS Appl. Mater. Interfaces* **2021**, *13* (13), 15761–15773. https://doi.org/10.1021/acsami.0c21961.

(17) Baggetto, L.; Unocic, R. R.; Dudney, N. J.; Veith, G. M. Fabrication and Characterization of Li-Mn-Ni-O Sputtered Thin Film High Voltage Cathodes for Li-Ion Batteries. *J. Power Sources* **2012**, *211*, 108–118. https://doi.org/10.1016/j.jpowsour.2012.03.076.

(18) Aziz, S.; Zhao, J.; Cain, C.; Wang, Y. Nanoarchitectured LiMn 2 O 4 /Graphene/ZnO Composites as Electrodes for Lithium Ion Batteries. *J. Mater. Sci. Technol.* **2014**, *30*, 427–433. https://doi.org/10.1016/j.jmst.2014.03.007.

(19) Hammad Fawey, M.; Chakravadhanula, V. S. K.; Reddy, M. A.; Rongeat, C.; Scherer, T.; Hahn, H.; Fichtner, M.; Kübel, C. In Situ TEM Studies of Micron-Sized All-Solid-State Fluoride Ion Batteries: Preparation, Prospects, and Challenges. *Microsc. Res. Tech.* **2016**, *79* (7), 615–624. https://doi.org/10.1002/jemt.22675.

(20) Bhattacharyya, R.; Frydman, L. Quadrupolar Nuclear Magnetic Resonance Spectroscopy in Solids Using Frequency-Swept Echoing Pulses. *J. Chem. Phys.* **2007**, *127* (19), 194503. https://doi.org/10.1063/1.2793783.

(21) Lutz, L.; Dachraoui, W.; Demortière, A.; Johnson, L. R.; Bruce, P. G.; Grimaud, A.; Tarascon, J. M. Operando Monitoring of the Solution-Mediated Discharge and Charge Processes in a Na-O2 Battery Using Liquid-Electrochemical Transmission Electron Microscopy. *Nano Lett.* **2018**, *18* (2), 1280–1289. https://doi.org/10.1021/acs.nanolett.7b04937.

(22) Masseboeuf, A. In Situ Characterization Methods in Transmission Electron Microscopy. **2013**, 199–218. https://doi.org/10.1002/9781118579022.ch8ï.

(23) Vitoux, L.; Reichardt, M.; Sallard, S.; Novák, P.; Sheptyakov, D.; Villevieille, C. A Cylindrical Cell for Operando Neutron Diffraction of Li-Ion Battery Electrode Materials. *Front. Energy Res.* **2018**, *6* (AUG). https://doi.org/10.3389/fenrg.2018.00076.

(24) Podor, R.; Ravaux, J.; Brau, H.-P. In Situ Experiments in the Scanning Electron Microscope Chamber. In *Scanning Electron Microscopy*; InTech, 2012. https://doi.org/10.5772/36433.

(25) Beaulieu, L. Y.; Cumyn, V. K.; Eberman, K. W.; Krause, L. J.; Dahn, J. R. A System for Performing Simultaneous in Situ Atomic Force Microscopy/Optical Microscopy Measurements on Electrode Materials for Lithium-Ion Batteries. *Rev. Sci. Instrum.* **2001**, *72* (8), 3313–3319. https://doi.org/10.1063/1.1388214.

(26) Baddour-Hadjean, R.; Pereira-Ramos, J. P. Raman Microspectrometry Applied to the Study of Electrode Materials for Lithium Batteries. *Chem. Rev.* **2010**, *110* (3), 1278–1319. https://doi.org/10.1021/cr800344k.

(27) Funke, C.; Chakrvadhanula, V. S. K. Characterisation of Battery Materials by Electron and Ion Microscopy Techniques: A Review. *Phys. Sci. Rev.* **2018**, *4* (3). https://doi.org/10.1515/PSR-2017-0153.

(28) Liu, S.; Xie, J.; Su, Q.; Du, G.; Zhang, S.; Cao, G.; Zhu, T.; Zhao, X. Understanding Li-Storage Mechanism and Performance of MnFe2O4 by in Situ TEM Observation on Its Electrochemical Process in Nano Lithium Battery. *Nano Energy* **2014**, *8*, 84–94. https://doi.org/10.1016/j.nanoen.2014.06.001.

(29) Liu, X. H.; Liu, Y.; Kushima, A.; Zhang, S.; Zhu, T.; Li, J.; Huang, J. Y. In Situ TEM Experiments of Electrochemical Lithiation and Delithiation of Individual Nanostructures. *Advanced Energy Materials*. John Wiley & Sons, Ltd July 1, 2012, pp 722–741. https://doi.org/10.1002/aenm.201200024.

(30) Wang, C. M. In Situ Transmission Electron Microscopy and Spectroscopy Studies of Rechargeable Batteries under Dynamic Operating Conditions: A Retrospective and Perspective View. *Journal of Materials Research*. Cambridge University Press February 14, 2015, pp 326–339. https://doi.org/10.1557/jmr.2014.281.

(31) Pu, S.; Gong, C.; Robertson, A. W. Liquid Cell Transmission Electron Microscopy and Its Applications. *Royal Society Open Science*. Royal Society Publishing January 1, 2020. https://doi.org/10.1098/rsos.191204.

(32) Wu, F.; Yao, N. Advances in Sealed Liquid Cells for In-Situ TEM Electrochemial Investigation of Lithium-Ion Battery. *Nano Energy*. Elsevier Ltd January 1, 2015, pp 196–210. https://doi.org/10.1016/j.nanoen.2014.11.004.

(33) Karakulina, O. M.; Demortière, A.; Dachraoui, W.; Abakumov, A. M.; Hadermann, J. In Situ Electron Diffraction Tomography Using a Liquid-Electrochemical Transmission Electron Microscopy Cell for Crystal Structure Determination of Cathode Materials for Li-Ion Batteries. *Nano Lett* **2018**, *18*, 3. https://doi.org/10.1021/acs.nanolett.8b02436.

(34) Huang, J. Y.; Zhong, L.; Wang, C. M.; Sullivan, J. P.; Xu, W.; Zhang, L. Q.; Mao, S. X.; Hudak, N. S.; Liu, X. H.; Subramanian, A.; et al. In Situ Observation of the Electrochemical Lithiation of a Single SnO 2 Nanowire Electrode. *Science* **2010**, *330* (6010), 1515–1520.

(35) Wang, F.; Yu, H. C.; Chen, M. H.; Wu, L.; Pereira, N.; Thornton, K.; Van Der Ven, A.; Zhu, Y.; Amatucci, G. G.; Graetz, J. Tracking Lithium Transport and Electrochemical Reactions in Nanoparticles. *Nature Communications* **2012**, *3*, 1201–1208.

(36) Cheng, Y.; Zhang, L.; Zhang, Q.; Li, J.; Tang, Y.; Delmas, C.; Zhu, T.; Winter, M.; Wang, M. S.; Huang, J. Understanding All Solid-State Lithium Batteries through in Situ Transmission Electron Microscopy. *Materials Today* **2021**, *42* (February), 137–161.

(37) Yamamoto, K.; Iriyama, Y.; Asaka, T.; Hirayama, T.; Fujita, H.; Fisher, C. A. J.; Nonaka, K.; Sugita, Y.; Ogumi, Z. Dynamic Visualization of the Electric Potential in an All-Solid-State Rechargeable Lithium Battery. *Angew. Chemie - Int. Ed.* **2010**, *49* (26), 4414–4417. https://doi.org/10.1002/anie.200907319.

(38) Wang, Z.; Santhanagopalan, D.; Zhang, W.; Wang, F.; Xin, H. L.; He, K.; Li, J.; Dudney, N.; Meng, Y. S. In Situ STEM-EELS Observation of Nanoscale Interfacial Phenomena in All-Solid-State Batteries. *Nano Lett.* **2016**, *16* (6), 3760–3767. https://doi.org/10.1021/acs.nanolett.6b01119.

(39) Unocic, R. R.; Jungjohann, K. L.; Mehdi, B. L.; Browning, N. D.; Wang, C. In Situ Electrochemical Scanning/Transmission Electron Microscopy of Electrode-Electrolyte Interfaces. *MRS Bulletin*. Cambridge University Press September 1, 2020, pp 738–745. https://doi.org/10.1557/mrs.2020.226.

(40) Brazier, A.; Dupont, L.; Dantras-Laffont, L.; Kuwata, N.; Kawamura, J.; Tarascon, J. M. First Cross-Section Observation of an All Solid-State Lithium-Ion “Nanobattery” by Transmission Electron Microscopy. *Chem. Mater.* **2008**, *20* (6), 2352–2359. https://doi.org/10.1021/cm7033933.

(41) Wang, Z.; Tang, Y.; Zhang, L.; Li, M.; Shan, Z.; Huang, J. In Situ TEM Observations of Discharging/Charging of Solid-State Lithium-Sulfur Batteries at High Temperatures. *Small* **2020**, *16* (28), 2001899. https://doi.org/10.1002/smll.202001899.

(42) Rauch, E. F.; Véron, M. Automated Crystal Orientation and Phase Mapping in TEM. *Mater. Charact.* **2014**, *98*, 1–9. https://doi.org/10.1016/j.matchar.2014.08.010.

(43) Thornton, J. A. The Microstructure of Sputter-deposited Coatings. *J. Vac. Sci. Technol. A Vacuum, Surfaces, Film.* **1986**, *4* (6), 3059–3065. https://doi.org/10.1116/1.573628.

(44) Wang, L.; Li, H.; Huang, X.; Baudrin, E. A Comparative Study of Fd-3m and P4332 “LiNi 0.5Mn1.5O4.” *Solid State Ionics* **2011**, *193* (1), 32–38. https://doi.org/10.1016/j.ssi.2011.04.007.

(45) Liu, D.; Han, J.; Goodenough, J. B. Structure, Morphology, and Cathode Performance of Li1-x[Ni0.5Mn1.5]O4 Prepared by Coprecipitation with Oxalic Acid. *J. Power Sources* **2010**, *195* (9), 2918–2923. https://doi.org/10.1016/j.jpowsour.2009.11.024.

(46) Baggetto, L.; Unocic, R. R.; Dudney, N. J.; Veith, G. M. Fabrication and Characterization of Li-Mn-Ni-O Sputtered Thin Film High Voltage Cathodes for Li-Ion Batteries. *J. Power Sources* **2012**, *211*, 108–118. https://doi.org/10.1016/j.jpowsour.2012.03.076.

(47) Aurbach, D. Review of Selected Electrode-Solution Interactions Which Determine the Performance of Li and Li Ion Batteries. *J. Power Sources* **2000**, *89* (2), 206–218. https://doi.org/10.1016/S0378-7753(00)00431-6.

(48) Xu, X. L.; Deng, S. X.; Wang, H.; Liu, J. B.; Yan, H. Research Progress in Improving the Cycling Stability of High-Voltage LiNi0.5Mn1.5O4 Cathode in Lithium-Ion Battery. *Nano-Micro Letters*. SpringerOpen April 1, 2017, p 22. https://doi.org/10.1007/s40820-016-0123-3.

(49) Vasile, M. J.; Nassar, R.; Xie, J.; Guo, H. Microfabrication Techniques Using Focused Ion Beams and Emergent Applications. *Micron* **1999**, *30* (3), 235–244. https://doi.org/10.1016/S0968-

4328(99)00008-6.

(50) Aziz, S.; Zhao, J.; Cain, C.; Wang, Y. Nanoarchitectured LiMn 2 O 4 /Graphene/ZnO Composites as Electrodes for Lithium Ion Batteries. *J. Mater. Sci. Technol.* **2014**, *30*, 427–433. https://doi.org/10.1016/j.jmst.2014.03.007.

(51) Fawey, M. H.; Chakravadhanula, V. S. K.; Munnangi, A. R.; Rongeat, C.; Hahn, H.; Fichtner, M.; Kübel, C. First Results from in Situ Transmission Electron Microscopy Studies of All-Solid-State Fluoride Ion Batteries. *J. Power Sources* **2020**, *466*, 228283. https://doi.org/10.1016/j.jpowsour.2020.228283.

(52) Vogt, P.; Capiod, P.; Berthe, M.; Resta, A.; De Padova, P.; Bruhn, T.; Le Lay, G.; Grandidier, B. Synthesis and Electrical Conductivity of Multilayer Silicene. *Appl. Phys. Lett.* **2014**, *104* (2), 021602. https://doi.org/10.1063/1.4861857.

(53) Watanabe, H.; Manabe, C.; Shigematsu, T.; Shimizu, M. Dual-Probe Scanning Tunneling Microscope: Measuring a Carbon Nanotube Ring Transistor. *Appl. Phys. Lett.* **2001**, *78* (19), 2928–2930. https://doi.org/10.1063/1.1371529.

(54) Kubo, O.; Shingaya, Y.; Nakaya, M.; Aono, M.; Nakayama, T. Epitaxially Grown WOx Nanorod Probes for Sub-100 Nm Multiple-Scanning-Probe Measurement. *Appl. Phys. Lett.* **2006**, *88* (25), 254101. https://doi.org/10.1063/1.2213954.

(55) Wang, B.; Idrissi, H.; Galceran, M.; Colla, M.; Turner, S.; Hui, S.; Raskin, J.; Pardoen, T.; Godet, S.; Schryvers, D. Advanced TEM Investigation of the Plasticity Mechanisms in Nanocrystalline Freestanding Palladium Films with Nanoscale Twins. *Int. J. Plast.* **2012**, *37*, 140–156. https://doi.org/10.1016/j.ijplas.2012.04.003.

(56) Izadi, E.; Darbal, A.; Sarkar, R.; Rajagopalan, J. Grain Rotations in Ultrafine-Grained Aluminum Films Studied Using in Situ TEM Straining with Automated Crystal Orientation Mapping. *Mater. Des.* **2017**, *113*, 186–194. https://doi.org/10.1016/j.matdes.2016.10.015.

(57) Mu, X.; Kobler, A.; Wang, D.; Chakravadhanula, V. S. K.; Schlabach, S.; Szabó, D. V.; Norby, P.; Kübel, C. Comprehensive Analysis of TEM Methods for LiFePO4/FePO4 Phase Mapping: Spectroscopic Techniques (EFTEM, STEM-EELS) and STEM Diffraction Techniques (ACOM-TEM). *Ultramicroscopy* **2016**, *170*, 10–18. https://doi.org/10.1016/j.ultramic.2016.07.009.

(58) Su, Z.; De Andrade, V.; Cretu, S.; Yin, Y.; Wojcik, M. J.; Franco, A. A.; Demortière, A. X-Ray Nanocomputed Tomography in Zernike Phase Contrast for Studying 3D Morphology of Li-O2Battery Electrode. *ACS Appl. Energy Mater.* **2020**, *3* (5), 4093–4102. https://doi.org/10.1021/acsaem.9b02236.

(59) Brunet, F.; Crouzet, C.; Cretu, S.; David, R.; Courty, M.; Demortière, A.; Recham, N. Oxidative Decomposition Products of Synthetic NaFePO4 Marićite: Nano-Textural and Electrochemical Characterization. *Eur. J. Mineral.* **2019**, *31* (4), 837–842. https://doi.org/10.1127/ejm/2019/0031-2885.

(60) Kim, J. H.; Huq, A.; Chi, M.; Pieczonka, N. P. W.; Lee, E.; Bridges, C. A.; Tessema, M. M.; Manthiram, A.; Persson, K. A.; Powell, B. R. Integrated Nano-Domains of Disordered and Ordered Spinel Phases in LiNi0.5Mn1.5O4 for Li-Ion Batteries. *Chem. Mater.* **2014**, *26* (15), 4377–4386. https://doi.org/10.1021/cm501203r.

(61) Kunduraci, M.; Al-Sharab, J. F.; Amatucci, G. G. High-Power Nanostructured $LiMn_{2-x}Ni_xO_4$ High-Voltage Lithium-Ion Battery Electrode Materials: Electrochemical Impact of Electronic

Conductivity and Morphology. *Chem. Mater.* **2006**, *18* (15), 3585–3592. https://doi.org/10.1021/cm060729s.

(62) (No Title) https://www.osti.gov/pages/servlets/purl/1430487 (accessed Nov 29, 2020).

(63) Xu, K. Nonaqueous Liquid Electrolytes for Lithium-Based Rechargeable Batteries. **2004**. https://doi.org/10.1021/cr030203g.

(64) Yang, L.; Ravdel, B.; Lucht, B. L. Electrolyte Reactions with the Surface of High Voltage LiNi 0.5Mn1.5O4 Cathodes for Lithium-Ion Batteries. *Electrochem. Solid-State Lett.* **2010**, *13* (8), A95. https://doi.org/10.1149/1.3428515.

(65) Zhan, C.; Wu, T.; Lu, J.; Amine, K. Dissolution, Migration, and Deposition of Transition Metal Ions in Li-Ion Batteries Exemplified by Mn-Based Cathodes-A Critical Review. *Energy and Environmental Science*. Royal Society of Chemistry February 1, 2018, pp 243–257. https://doi.org/10.1039/c7ee03122j.

(66) Yan, P.; Zheng, J.; Xiao, J.; Wang, C. M.; Zhang, J. G. Recent Advances on the Understanding of Structural and Composition Evolution of LMR Cathodes for Li-Ion Batteries. *Frontiers in Energy Research* **2015**, *3* (JUN), 1–10. https://doi.org/10.3389/fenrg.2015.00026.

(67) Xiao, B.; Liu, H.; Liu, J.; Sun, Q.; Wang, B.; Kaliyappan, K.; Zhao, Y.; Banis, M. N.; Liu, Y.; Li, R.; et al. Nanoscale Manipulation of Spinel Lithium Nickel Manganese Oxide Surface by Multisite Ti Occupation as High-Performance Cathode. *Advanced Materials* **2017**, *29* (47), 1–12. https://doi.org/10.1002/adma.201703764.

(68) Berthe, M.; Durand, C.; Xu, T.; Nys, J. P.; Caroff, P.; Grandidier, B. Combined STM and Four-Probe Resistivity Measurements on Single Semiconductor Nanowires; Springer, Berlin, Heidelberg, 2012; pp 107–118. https://doi.org/10.1007/978-3-642-28172-3_8.